Field comparison of dry deposition samplers for collection of atmospheric mineral dust: results from single-particle characterization

Andebo Waza[1], Kilian Schneiders[1], Jan May[2], Sergio Rodríguez[3, 4], Bernd Epple[2], Konrad Kandler[1]

1Atmospheric Aerosol, Institute for Applied Geosciences, Technische Universität Darmstadt, D-64287 Darmstadt, Germany

2Institute for Energy Systems & Technology, Technische Universität Darmstadt, D-64287 Darmstadt, Germany

3Izaña Atmospheric Research Centre, AEMET, Tenerife, Spain.

4Estación Experimental de Zonas Aridas, EEZA CSIC, Almería, Spain.

*correspondence to andebo.waza@geo.tu-darmstadt.de

Abstract

Frequently, passive dry deposition collectors are used to sample atmospheric dust deposition. However, there exists a multitude of different instruments with different, usually not well-characterized sampling efficiencies. As a result, the acquired data might be considerably biased with respect to their size representativity, and as consequence, also composition. In this study, individual particle analysis by automated scanning electron microscopy coupled with energy-dispersive X-ray was used to characterize different, commonly used passive samplers with respect to their size-resolved deposition rate and concentration. This study focuses on the microphysical properties, i.e. the aerosol concentration and deposition rates as well as the particle size distributions. In addition, computational fluid dynamics modeling was used in parallel to achieve deposition velocities from a theoretical point of view.

SEM calculated deposition rate measurements made using different passive samplers show a disagreement among the samplers. Modified Wilson and Cooke (MWAC) and Big Spring Number Eight (BSNE) - both horizontal flux samplers - collect considerably more material than Flat plate and the Sigma-2, which are vertical flux samplers. The collection efficiency of MWAC increases for large particles in comparison to Sigma-2 with increasing wind speed, while such an increase is less observed in the case of BSNE. A positive correlation is found between deposition rate and PM_{10} concentration measurements by an optical particle spectrometer. The results indicate that a BSNE and Sigma-2 can be good options for PM_{10} measurement, whereas MWAC and Flat plate samplers are not a suitable choice. A negative correlation was observed in between dust deposition rate and wind speed. Deposition velocities calculated from different classical deposition models do not agree with deposition velocities estimated using computational fluid dynamics simulations (CFD). The deposition velocity estimated

31 from CFD was often higher than the values derived from classical deposition velocity models. Moreover,

32 the modeled deposition velocity ratios between different samplers do not agree with the observations.

33 **Key words**: Mineral dust particles, passive samplers, SEM-EDX, single particle analysis, computational

34 fluid dynamics

1   Introduction

36 Mineral dust aerosol in the climate system has received considerable scientific attention mainly due to

37 its direct effect on the radiative budget and indirect one on cloud microphysical properties (Arimoto,

38 2001; Huang et al., 2010). Mineral dust particles also play a key part with respect to gas phase chemistry

39 by providing a reaction surface e.g. ozone depletion (Nicolas et al., 2009; Prospero et al., 1995).

40 Moreover, dust aerosol also plays an important role in biogeochemical cycles by supplying important

41 and limiting nutrients to Ocean surfaces (Jickells et al., 2005). Mineral dust is emitted mainly from the

42 arid and semi-arid regions of the world and believed to have a global source strength ranging from 1000-

43 3000 Tgyr^{-1} (Andreae, 1995). They form the single largest component of global atmospheric aerosol mass

44 budget, contributing about one third of the total natural aerosol mass annually (Penner et al., 2001).

45 Deposition measurement data of mineral dust are useful to validate numerical simulation models and to

46 improve our understanding of deposition processes. However, the scarcity and the limited

47 representatively of the deposition measurement data for validation pose a major challenge to assess dust

48 deposition at regional and global scales (Schulz et al., 2012; WMO, 2011). This is in part linked to the

49 uncertainties evolving from the use of different and non-standardized measurement techniques.

50 Commonly, deposition is measured by passive techniques, which provide an acceptor area for the

51 depositing atmospheric particles. The advantage of these passive samplers is that they operate passively,

52 resulting in simple and thus cheaper instruments, so that many locations can be sampled at a reasonable

53 cost (Goossens and Buck, 2012). The usual lack of a power supply allows also for unattended remote

54 setups. However, the most important disadvantage is that collection efficiency and deposition velocity is

55 determined by the environmental conditions not under operator control, and in remote setups also

56 frequently also unknown. That implies, in addition, that the sampler shape can have a strong and variable

57 impact of the collection properties.

58 While there is previous work describing and modeling single samplers (Einstein et al., 2012; Wagner and

59 Leith, 2001a, b; Yamamoto et al., 2006) and a few comparison studies (Goossens and Buck, 2012;

60 Mendez et al., 2016), most previous studies (Goossens and Buck, 2012; López-García et al., 2013) only

61 compare total mass, thereby neglecting size dependence and potential comparison biases. Also, a

62 systematic assessment of the impact of wind conditions is not commonly carried out, but for example

63 Mendez et al. (2016) showed that the efficiency of the BSNE and MWAC samplers for collecting PM_{10}

64 varies with wind speed, and Goossens and Buck (2012) found that PM_{10} concentrations from BSNE and

65 DustTrak samplers have comparable values for wind speeds from 2–7 m/s.

66 The purpose of this study is to assess the particle collection properties of different deposition and other

67 passive samplers based on single particle measurements, and to assess their agreement with theory. From

68 the available data, also relations of the collected particle microphysics and composition homogeneity

69 between the samplers will be presented, which can be used as estimators for the comparability of previous

70 literature data based on the different techniques. To the best of our knowledge, this is the first study to

71 analyze dry deposition measurements collected using passive samplers by means of a single-particle

72 SEM-EDX Analysis approach (particularly in the size fraction larger than 10 μm).

73 ## 2   Material and methods

74 **2.1   Sampling location and time**

75 Sahara and Sahel provide large quantities of soil dust, resulting in a westward flow of mineral dust

76 particles over the North Atlantic Ocean accounting for up to 50% of global dust budget (Goudie and

77 Middleton, 2001). Owing to proximity to the African continent, the Canary Islands are influenced by dust

78 particles transported from Sahara and Sahel regions. Therefore, Tenerife is one of the best locations to

79 study relevant dust aerosol in a natural environment.

80 For this study, we conducted a two month (July to August 2017) aerosol collection and dry deposition

81 sampling campaign at Izaña Global Atmospheric Watch observatory (Bergamaschi et al., 2000;

82 Rodríguez et al., 2015) (28.3085ºN, 16.4995ºW). Sampling inlet were placed at a height of 2 m above

83 ground, on top of a measurement installation. The installation was made on a 160 m^2 flat concrete

84 platform. The trade wind inversion, which is a typical meteorological feature of the station, shields most

85 of the time the observatory from local island emissions (García et al., 2016). Therefore, the Izaña Global

86 Atmospheric Watch observatory is an ideal choice for in-situ measurements under "free troposphere"

87 conditions (Bergamaschi et al., 2000; García et al., 2016).

2.2 Wind measurements

An ultra-sonic anemometer (Young model 81000, R. M. Young Company, Traverse City, MI, USA) was installed at approximately 2 m height above the ground to obtain the 3-D wind velocity and direction. It was operated with a time resolution of 10 Hz to get basic information on turbulence structure.

2.3 Particle sampling

Samples were collected from different, commonly used samplers, namely Big Spring Number Eight (BSNE) (Fryrear, 1986), Modified Wilson and Cooke (MWAC) (Wilson and Cook, 1980), Sigma-2 (VDI2119, 2013) and Flat plate (UNC-derived) (Ott and Peters, 2008). In addition, the free-wing impactor (FWI) (Kandler et al., 2018) was used to collect coarser particles. The BSNE, MWAC, FWI and Filter Sampler were mounted on wind vanes to align them to the ambient wind direction. Samples were collected continuously, and substrates were exchanged at intervals of 24 hours. The sampling duration for FWI (12 mm Al-stub) was 30 min only to avoid overloading. The sampling duration for filter sampler was set to be one hour. It has to be noted that the PM_{10} from optical measurements for this particular 0.5 or 1 hour only deviates by 2 % and 0.2 % respectively from the 24-h-average.

2.3.1 Dust deposition samplers

2.3.1.1 Flat plate sampler

The Flat plate sampler used in this work was taken from the original Flat plate geometry used in Ott and Peters (2008). Briefly, the geometry contains two round brass plates (top plate diameter 203 mm, bottom plate 127 mm, thickness 1 mm each) mounted in a distance of 16 mm. Unlike the original design, the geometry of the current work has a cylindrical dip in the lower plate, which recedes the sampling substrate – a SEM stub with a thickness of 3.2 mm – from the airflow, thereby reducing the flow disturbance. A preliminary study with the modified and original setup side-by-side in a rural environment had shown that this recession approximately doubles the collection efficiency for large particles. In this design, larger droplets (> 1 mm) are prevented by this setup from reaching the SEM stub surface at the local wind speeds Ott and Peters (2008). As described in Wagner and Leith (2001a); (Wagner and Leith, 2001b), the main triggers for particle deposition on the substrates for this sampler are diffusion, gravity settling, and turbulent inertial forces, of which only the latter two are relevant in our study.

2.3.1.2 Upward-downward deposition rate sampler

It is important to compare the upward and downward rates to understand the turbulent and the gravitational share in aerosol deposition rate measurement. Following an approach by Noll and Fang (1989), it was assumed that turbulent transport is the main mechanism for upward-directed deposition rate while turbulent transport and sedimentation are the mechanism of for the downward one. Therefore,

120 a sampler with an upward- and a downward-facing substrate in analogy to the Flat plate sampler was

121 designed. Air is flowing between two circular steel plates thick 1 mm with a diameter of 127 mm. In the

122 centers of the plates, two substrates are mounted opposite to each other. The substrate holders are

123 recessed, so that their adhesive collection surface is in plane with the steel surface. The construction is

124 mounted into a frame with a distance of 16 mm between the plates / substrates.

125 2.3.1.3   Sigma-2 sampler

126 The Sigma-2 sampling device is described in Dietze et al. (2006); (Schultz, 1989; VDI2119, 2013).

127 Briefly, the geometry consists of a cylindrical sedimentation tube with a height of about 27 cm made of

128 antistatic plastic, which is topped by a protective cap with diameter of 158 mm. At its top, the cap has

129 four rectangular inlet windows (measuring 40 mm x 77 mm, all at the same height) at its side providing

130 away for passive entrance of particles to the collection surface. Once entered the tube, particles are

131 assumed settle down to the collection surface due to gravitation (Stokes' law) (VDI2119, 2013). The

132 samplers designed in a way that it protects the sample from direct radiation, wind and precipitation.

133 2.3.1.4   The Modified Wilson and Cooke (MWAC) sampler

134 The MWAC sampler is based on an original design developed by Wilson and Cook (1980). The sampler

135 consists of a closed polyethylene bottle, serving as settling chamber, to which an inlet tube and an outlet

136 tube have been added. The MWAC sampling bottles are 95 mm long with a diameter of 48 mm. The two

137 inlet and outlet plastic tubes with inner and outer diameter 8 and 10 mm respectively, pass air through

138 the cap into the bottle and then out again. The large volume of the bottle relative to the inlet diameter

139 makes the dust particles entering the bottle to be deposited in the bottle due to the flow deceleration the

140 total bottle area, and due to impaction below the exit of the inlet tube. The air then discharges from the

141 bottle via the outlet tube. MWAC is one of the most commonly used samplers (Goossens and Offer,

142 2000) and has a high sampling efficiency for large particles (Mendez et al., 2016).

143 2.3.1.5   The Big Spring Number Eight (BSNE) sampler

144 The BSNE sampler, originally designed by Fryrear (1986), is intended to collect airborne dust particles

145 from the horizontal flux (Goossens and Offer, 2000). Briefly, the particle laden air passes through a

146 rectangular inlet (21 mm wide and 11 mm high, with total area of 231 mm^2). Once inside the sampler,

147 air speed is reduced by continuous cross section increase (angular walls) and the particles settle out on a

148 collection surface. Air discharges through a mesh screen.

149   2.3.2   Free-wing impactor (FWI)

150   A free rotating wing impactor (Jaenicke and Junge, 1967; Kandler et al., 2018; Kandler et al., 2009) was
151   used to collect particles larger than approximately 5 µm. A FWI has a sticky impaction surface attached
152   to a rotating arm that moves through air; particles deposit on the moving plate due to their inertia. The
153   rotating arm is moved at constant speed by a stepper motor, which is fixed on a wind vane, aligning the
154   FWI to wind direction. The particle size cut-off is defined by the impaction parameter, i.e. by rotation
155   speed, wind speed and sample substrate geometry. Details of working principle of FWI can be obtained
156   from Kandler et al. (2018)

157   2.3.3   Filter sampler

158   A filter sampler with Nucleopore filters (Whatman® Nuclepore™ Track-Etched Membranes diam. 25
159   mm, pore size 0.4 µm, polycarbonate) mounted on a wind vane was used for iso-axial particle collection.
160   An inlet nozzle of 6 mm was used to achieve pseudo-isokinetic conditions. Sample flow (0.75 m³/h
161   volumetric at ambient conditions) was measured by a mass flow meter (MASS-STREAM, M+W
162   instruments, Leonhardsbuch, Germany). The filter sampler was operated at least two times a day.

163   **2.4   Ancillary Aerosol Data**
164   Additional information regarding the aerosol particle size distributions has been obtained by using an
165   optical particle counter (OPC, GRIMM, Ainring, Germany), which is operationally available at the Izaña
166   Global Atmospheric Watch observatory (Bergamaschi et al., 2000; Rodríguez et al., 2015).

167   **2.5   SEM-Analysis**
168   All aerosol samples (except the filter sampler) were collected on pure carbon adhesive substrates (Spectro
169   Tabs, Plano GmbH, Wetzlar, Germany) mounted to standard SEM aluminum stubs. The filter samples
170   were stored in standard 'Petrislides' (Merck KGaA, Darmstadt, Germany). All adhesive samples were
171   stored in standard SEM storage boxes (Ted Pella Inc, Redding, CA, USA) in dry conditions at room
172   temperature. Individual particle analysis by automated scanning electron microscopy (SEM; FEI ESEM
173   Quanta 400 FEG, FEI, Eindhoven, The Netherlands; operated at 12.5 kV, lateral beam extension 3 nm
174   approx., spatial resolution 160 nm) was used to characterize particles for size and composition. A total
175   of 316,000 particles from six samplers was analyzed. 26 samples from BSNE (53,000 particles), 23
176   samples from MWAC (49,000), 23 samples from SIGMA-2 (39,000), 18 samples from Flat plate (12
177   mm) (24,000), 22 samples from Flat plate (25 mm) (21,000), 13 samples from Filter (80,000) and 12
178   samples from FWI-12 mm (50,000) were analyzed. Each sample was characterized at areas selected by
179   a random generator, until a total of 3,000 particles with projected area diameters greater than 1 µm was

reached. For particle identification, the backscattered electron image (BSE-image) has been used, as dust particles contain elements with higher atomic number than carbon and therefore appear as detectable bright spots in the BSE-image.

Chemistry information was derived by energy-dispersive X-ray analysis (EDX; Oxford X-Max 120, Oxford Instruments, Abingdon, United Kingdom). The internal ZAF-correction of the detector / software system – based on inter-peak background radiation absorption measurements for correction – was used for obtaining quantitative results.

2.6 Particle size determination

The image analysis integrated into the SEM-EDX software determines the size of particles as a projected area diameter.

$$\mathbf{d_g} = \sqrt{\frac{4B}{\pi}} \tag{1}$$

Where $\mathbf{B}$ and $\boldsymbol{d_g}$ are the area covered by the particle on the sample substrate and the projected area diameter respectively.

Following Ott et al. (2008), the volumetric shape factor, $\boldsymbol{S_v}$ is determined from the count data as:

$$\boldsymbol{S_v} = \frac{P^2}{4\pi A} \tag{2}$$

Where P and A are the perimeter and the projected area of the particle respectively.

The volume-equivalent diameter (sphere with the same volume as the irregular shaped particle) is then, calculated from the projected area diameter via the volumetric shape factor (Ott et al., 2008) and is expressed by particle projected area and perimeter as

$$\boldsymbol{d_v} = \frac{4\pi B}{P^2} dg = \frac{1}{P^2}\sqrt{64\pi B^3} \tag{3}$$

The aerodynamic diameter (d_a) is calculated from projected area diameter through the use of a volumetric shape factor and aerodynamic shape factor (Wagner and Leith, 2001b)

$$d_a = \sqrt{[\boldsymbol{d_v}\,(\boldsymbol{\rho_p}/\boldsymbol{\rho_0})\mathbf{1}/\boldsymbol{S_d})]} \tag{4}$$

With $\boldsymbol{S_d}$ the aerodynamic shape factor; $\boldsymbol{\rho_p}$ and $\boldsymbol{\rho_0}$ are particle density and unit density respectively. For this work, a value of $S_d = 1.41$ was used (Davies, 1979). Cunningham's slip correction was neglected in this study, as all particles considered were super-micron size.

2.7 Mass and number deposition rate calculation

The mass deposition rate (MDR) and number deposition rate (NDR) are calculated from deposited particle numbers per area, individual particle size and, in case of MDR, density. The particle density was assumed to be equal the bulk material density of the dominating identified compound for each particle (Kandler et al., 2007). A window correction (Kandler et al., 2009) was applied to the particle deposition rate as:

$$C_w = \frac{w_x w_y}{(w_x - d_p)(w_y - d_p)} \tag{5}$$

Where w_x and w_y are the dimensions of the analysis rectangle.

The MDR of the samples is then determined as

$$MDR = \frac{1}{Ati} \sum_k \rho \, d_p^3 C_w(d_p, k) \tag{6}$$

Similarly, The NDR of the samples is determined as

$$NDR = \frac{1}{Ati} \sum_k C_w(d_p, k) \tag{7}$$

With A is the total analyzed area, t is the sample collection time, ρ particle density and k is index of the particle.

Size distributions for all properties were calculated for the logarithmic-equidistant intervals of 1-2 μm, 2-4 μm, 4-8 μm, 8-16 μm, 16-32 μm, and 32-64 μm.

2.8 Modeling atmospheric concentrations and size distributions from flux measurements

Concentrations are calculated from the deposition rate using different deposition velocity models for different samples, namely the models of Stokes and Piskunov (Piskunov, 2009). The basic relationship between concentration and deposition rate was already given by Junge (1963), as the ratio of deposition rate to concentration:

$$V_d = F/C \tag{8}$$

With F is deposition rate and C is concentration. Note that the formulation is independent of the type of concentration, i.e. it can be equally applied to number or mass concentrations.

All different approaches now give different formulations for the deposition velocity, based on a set of assumptions and neglections.

233 2.8.1   Stokes settling

234 Terminal settling velocity (V_{ts}) is calculated according to Stokes' law.

235 $$V_{ts} = \frac{d_p^2 g (\rho_p - \rho_a)}{18\mu}$$ **(9)**

236 Where d_P is the particle size, g is the gravitational acceleration (9.81 m/s^2); $\boldsymbol{\rho_p}$ the density of particle; $\boldsymbol{\rho_a}$

237 the air density; μ is the dynamic viscosity of air ($1.8*10^{-5}$ kg/(ms)).

238 2.8.2   Turbulent deposition and more complex deposition models

239 To calculate the turbulent impaction velocity, which depends of the wind speed, the friction velocity is

240 needed. Friction velocity (u_*), which is a measure of wind generated turbulence is one most important

241 variables affecting deposition velocity (Arya, 1977). Mainly two different approaches have been used to

242 estimate u_*. On one hand the momentum flux or the eddy covariance (EC) approach (Ettling, 1996),

243 which directly estimates u_* from the correlations between the measured horizontal and vertical wind

244 velocity fluctuation, and on the other the law of the wall (LoW) approach (Shao et al., 2011), which

245 estimates u_* from the wind profile. The latter can be approximated from free-stream velocity and

246 roughness assumptions (Wood, 1981), where the flow inside the sampler is assumed to be in the

247 hydraulically smooth regime (Schlichting, 1968). **Figure 1** shows correlations between u_* estimated

248 using Wood (1981) and Ettling (1996) approaches. Obviously, the approaches lead to different results,

249 for which no clear explanation is available (Dupont et al., 2018) .
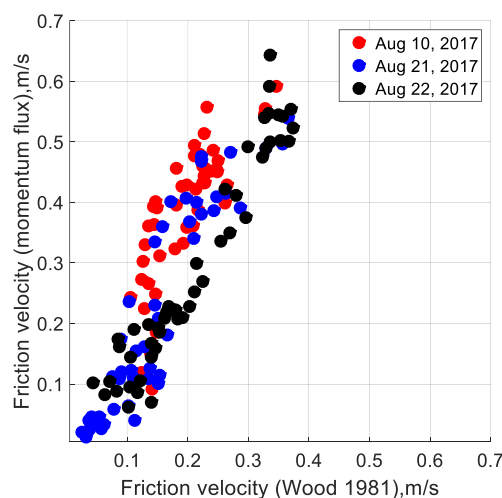
250

251 **Figure 1**: Comparison of the friction velocities obtained from the momentum flux and the Wood 1981

252 approaches for different days with different wind speeds (average wind speed =2.9 m/s, 2.1 m/s, 3.1

253 m/s for Aug 10, Aug 21, and Aug 22, 2017, respectively).

254 For the current work, the friction velocity is calculation is based on Wood (1981) approach:

255 $u_* = (u/\sqrt{2}) \, [(2log10(Re) - 0.65)^{-1.15}]$ **(10)**

256 Where Re is the flow Reynolds number at the sampling stub location and is given as

257 $Re = uX/V$ **(11)**

258 X is the distance from the lower plate edge to the center of the sampling stub (6.3 cm) and V is kinematic

259 viscosity.

260 The reason why we opted to use the Wood (1981) over the Ettling (1996) approach is a) its simplicity, as

261 it requires only average wind speeds instead of 3D high resolution ones, and therefore will be more

262 commonly applicable; and b) the fact that the momentum approach yields sometimes uninterpretable

263 data, in particular in case of buoyancy-driven flow. For some case studies, both approaches are compared

264 below.

265 There are a variety of models estimating the particles deposition speed (Aluko and Noll, 2006; Noll and

266 Fang, 1989; Noll et al., 2001; Piskunov, 2009; Slinn and Slinn, 1980; Wagner and Leith, 2001a) (see

267 **Figure 2**). And these different deposition velocity models yield different results, which could be due to

268 negligence of unaccounted forces (Lai and Nazaroff, 2005) or due to the way how friction velocity is

269 determined or can be related to suppositions by different models (Kandler et al., 2018). Unless otherwise

270 stated, the particle density used in deposition velocity calculation is 2600 kg/m^3.

271 It can be noted that a particular deposition model therefore may not be suitable in different cases for

272 describing the deposition velocity precisely, so as a result concentrations derived from deposition rate

273 measurements are likely to be biased (Giardina and Buffa, 2018; Kandler et al., 2018).
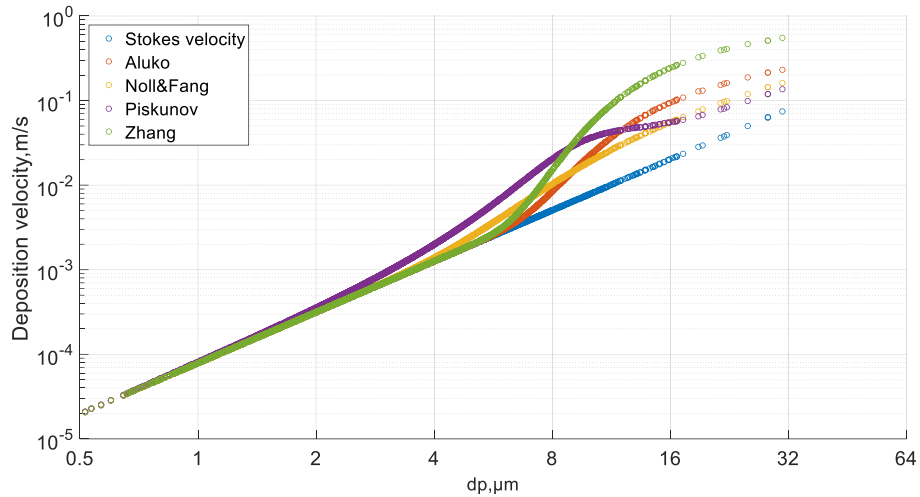
Figure 2: Deposition velocities for single particles to a smooth surface (Flat plate sampler) calculated by using set of different classical deposition models for Tenerife samples (Aug 9, 2017; average wind speed =3.0 m/s).

2.8.3 Deposition models applied to the samplers

Table 1 shows the different deposition velocity models applied to the various samplers. The Piskunov deposition velocity model is made for flat surfaces, and therefore it is applied to BSNE and Flat plate, where deposition occurs to such surfaces. For the Sigma-2 sampler, it is assumed that each particle settles with the terminal settling velocity (Tian et al., 2017), and therefore Stokes' velocity was used for calculation of concentrations. In the case of MWAC, a different approach was required due to its geometry. It is internally in principle an impactor design with the incoming tube pointing at the substrate, but is operating at very low flow speed and therefore Reynolds numbers. As a result, it cannot be described by the impactor theory only. Therefore, we assumed that the deposition velocity can't become smaller than the one prescribed by the Piskunov model. As a result, we derived a velocity model based on wind speed (or a reduced wind speed) and calculated the collection efficiency assuming the MWAC to act as impactor for particles in the range of the cut-off diameter and larger. For smaller particles, we assumed that flow is like a flow over a smooth surface, so the Piskunov deposition velocity model was applied (e.g., as soon as the deposition velocity from impactor considerations becomes smaller than the Piskunov one, the latter was used).

Table 1: A summary of different deposition velocity models applied to the samplers

Sampler	Deposition velocity model
Sigma-2	Stokes' velocity
Flat plate	Piskunov
BSNE	Piskunov
MWAC	Combination of Piskunov and Impaction curve

2.9 Determining the size distributions for mass concentration from the free-wing impactor measurements

Considering the windows correction and the collection efficiency dependence on the impaction speed and geometry, the overall collection efficiency E is calculated according to Kandler et al. (2018). After calculating the collection efficiency, the atmospheric concentration is calculated from deposition rate and deposition velocity as

$$C = \frac{M}{V_d} = \frac{M}{E \, V_{imp}} \qquad (12)$$

With E being the collection efficiency and v_imp the impaction velocity, calculated from ambient wind speed and rotation speed.

2.10 Determining the size distributions for mass concentration from the filter sampler measurements

Apparent number concentrations are determined from the particle deposition rate and the volumetric flow rate calculated from the mass flow for ambient conditions. The inlet efficiency (Eff_{in}) – accounting for the sampling biased caused by the difference in wind speed and inlet velocity – is calculated (Belyaev and Levin, 1974). The ambient concentration N_{out} is calculated by dividing the measured number concentration by the inlet efficiency. The effect for the regarded particles size, however, is small in comparison to the differences between the samplers.

2.11 Statistical uncertainty

Owing to the discrete nature of the particle size measurement, the uncertainty coming from counting can pose a significant contribution to the uncertainty of mass deposition rate measurement (Kandler et al., 2018). It is, therefore, important to assess the uncertainties in our mass deposition rate measurements, which is done in accordance to the previous work (Kandler et al., 2018). For the mass deposition rate, the statistical uncertainty is assessed by a bootstrap simulation approach using Monte Carlo

approximation (Efron, 1979). In this work, the bootstrap simulations and the two-sided 95 % confidence intervals calculation were performed by using Matlab's bootstrap function (MATLAB R2016a (MathWorks, Inc). Here, MATLAB function uses a non-parametric bootstrap algorithm (Neto, 2015) to compute the 95% bootstrap confidence interval.

3   Computational fluid dynamics (CFD) simulation

Computational fluid dynamics (CFD) simulations were conducted to predict the deposition of particles on to different passive samplers (MWAC, Sigma-2 and Flat plate). A discrete phase model without interaction with continuous phase was used to calculate the trajectories of the particles. The CFD software ANSYS-FLUENT 18.2 was used for performing the numerical simulations.

3.1   Evaluating the mean flow field

In a first step the geometry of samplers was created using ANSYS DesignModeler. In a second step, an enclosure around the geometry was generated. To ensure that there are no large gradients normal to the boundaries at the domain boundary, the domain was created depending on the width, the height and the length of the geometries. The space in front of the geometry is two times the height of the sampler, the space behind the sampler is ten times the height, the space left and right of the geometry is five times the width of the geometry and the space below and above the sampler is five times the height.

Afterwards a mesh was created using the ANSYS Meshing program. For the enhanced wall treatment the first near-wall node should be placed at the dimensionless wall distance of $y^{+\wedge}\approx 1$. The dimensionless wall distance is given by

$$y^+ = \frac{u_* y}{v} \tag{13}$$

With y the distance to the wall, v the kinematic viscosity of the fluid and u_* the friction velocity which is defined for this purpose by

$$u_* = \sqrt{\tau_w/\rho} \tag{14}$$

With τ_w the wall, shear stress and ρ the fluid density at the wall. The wall is then subdivided into a viscosity-affected region and a fully turbulent region depending on the turbulent Reynolds number Re_y

$$Re_y = \frac{\rho y \sqrt{k}}{\mu} \tag{15}$$

345 With y the wall-normal distance from the wall to the cell centers, k the turbulence kinetic energy and μ

346 the dynamic viscosity of the fluid. If $Re_y > 200$ the k-epsilon model is used. $Re_y < 200$ the one-equation

347 of Wolfstein is employed (Chmielewski and Gieras, 2013; Fluent, 2015). The flow field was calculated

348 by solving the Reynolds Averaged Navier Stokes's equations with the software ANSYS Fluent. Standard

349 k-epsilon model was used to calculate the Reynolds-stresses. The boundary conditions at the sides of the

350 domain were set to symmetric. The inlet boundary condition was set to 2, 4 or 8 m/s with air as fluid

351 (Density: 1.225 kg/m^3, viscosity: 1.7849*10^{-5} kg/(ms)). The outlet boundary condition was set to pressure

352 outlet.

353 The turbulence intensity $\mathbf{T_i}$ was calculated as

354 $$\mathbf{T_i} = \frac{\left(\frac{2}{3}\mathbf{k}\right)^{1/2}}{\mathbf{v}} \qquad (16)$$

355 With k the turbulence intensity and v the velocity at the inlet of the domain.

356 Detail of the sampler construction and geometry are found in the electronic supplement (see **Figure S**

357 **24, S 25** and **S 26**). Different cases were calculated for the Flat plate sampler (deposition area of 12 and

358 25 mm), for the Sigma-2 and for the MWAC (**Figure 3**). For the Flat plate, a mesh with 3,920,000 cells

359 was generated, for the Sigma-2 one with 7,600,000 cells and for the MWAC one with 4,620,000. After

360 the meshing, the flow fields were calculated. **Figure 3** shows as example the velocity magnitude in the

361 middle of the domain for a velocity of 4 m/s at the inlet.

362 In the last step, particles were injected into the velocity field and their trajectories computed. For all

363 samplers, the deposition area boundary condition was set to "trap" and the walls were defined as

364 reflecting boundaries. Different particle sizes (1, 2.5, 5, 10, 20 and 50 μm, Stokes' diameter) for three

365 different wind speeds (2, 4, 8 m/s) were investigated. The particles density was set to a value of 2600

366 kg/m³ to match an approximate dust bulk density. The particle concentration was $4*10^8$ /m^2 in all cases,

367 while the injection area was adjusted to the geometries (**Figure 3**).

368 The number of particles trapped in the deposition area was determined. The deposition velocity V_d was

369 calculated by

370 $$V_d = \frac{N_{pt}v}{A_d C_p} \qquad (17)$$

371 with N_{pt} the number of trapped particle at the deposition area, v the velocity of the air at the inlet

372 boundary of the domain, A_d the deposition area and C_p the particle concentration at the particle injection

373 area (Sajjadi et al., 2016).

374
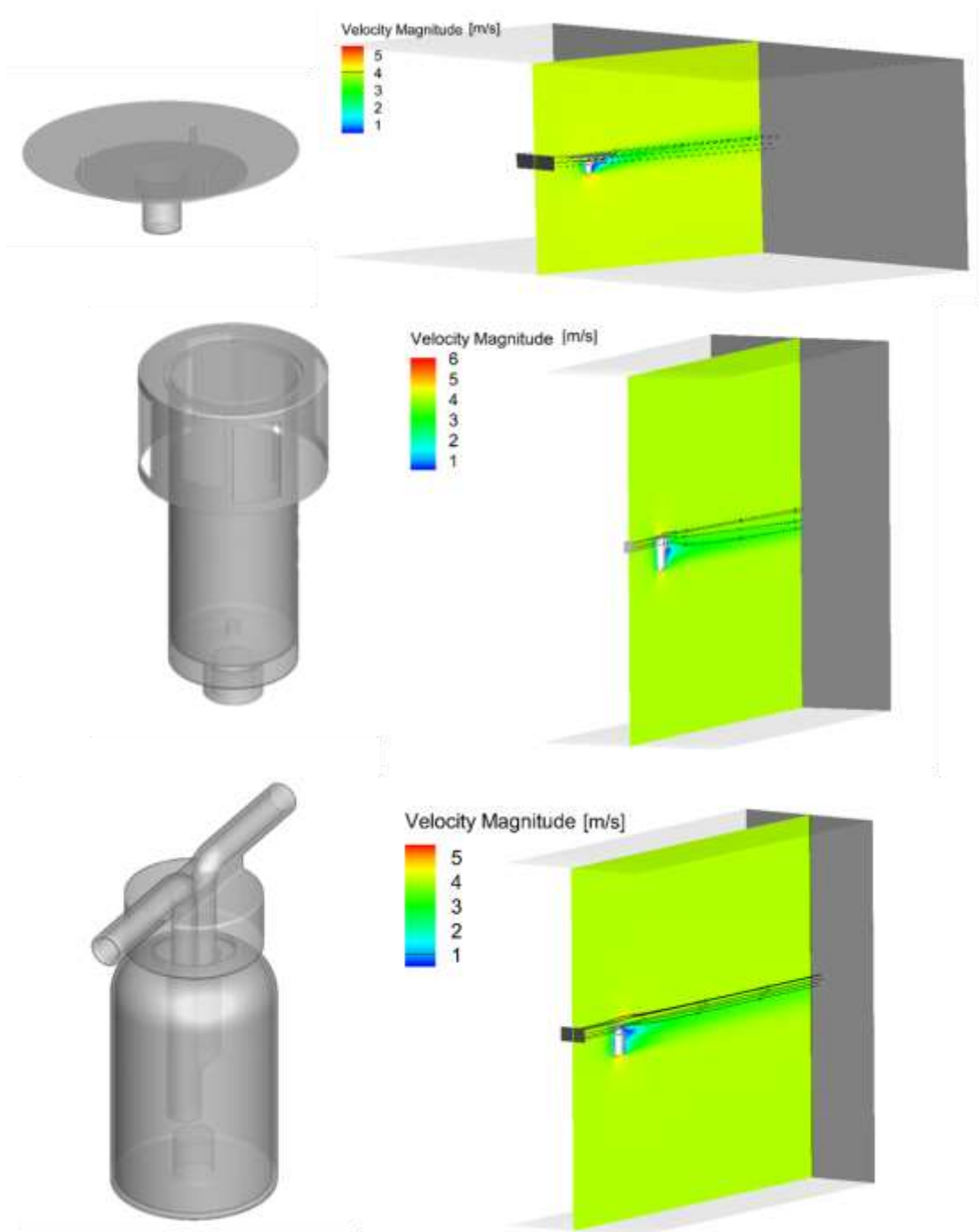
375

376   **Figure 3**: Geometries of Flat plate sampler (top), Sigma-2 sampler (middle), MWAC sampler (bottom).

377   CFD modeling domain and velocity magnitude, inlet velocity: 4 m/s (right); in addition, the injection

378   area is shown in black (Flat plate sampler: width 0.2 m, height 0.05 m; Sigma-2-sampler: width 0.2 m,

379   height 0.1 m; Bottle sampler: width 0.1 m, height 0.05 m) along with exemplary streamtraces.

3.2   Velocity contours and vectors for the samplers

For the Flat plate sampler, stream velocities and turbulence intensities are shown in **Figure 4**. The formation of the boundary layer at the wall of the sampler is clearly visible at all velocities. At the central sampling location, the flow between the plates has the same velocity as the free stream, so for the analytical deposition models, the lower plate can be treated as single surface. The highest velocity is found at the sharp edge at the bottom of the sampler. Due to the high velocity gradients in this part there is also the highest turbulence intensity in the domain. As expected, the turbulent wake becomes smaller with increasing wind speed.
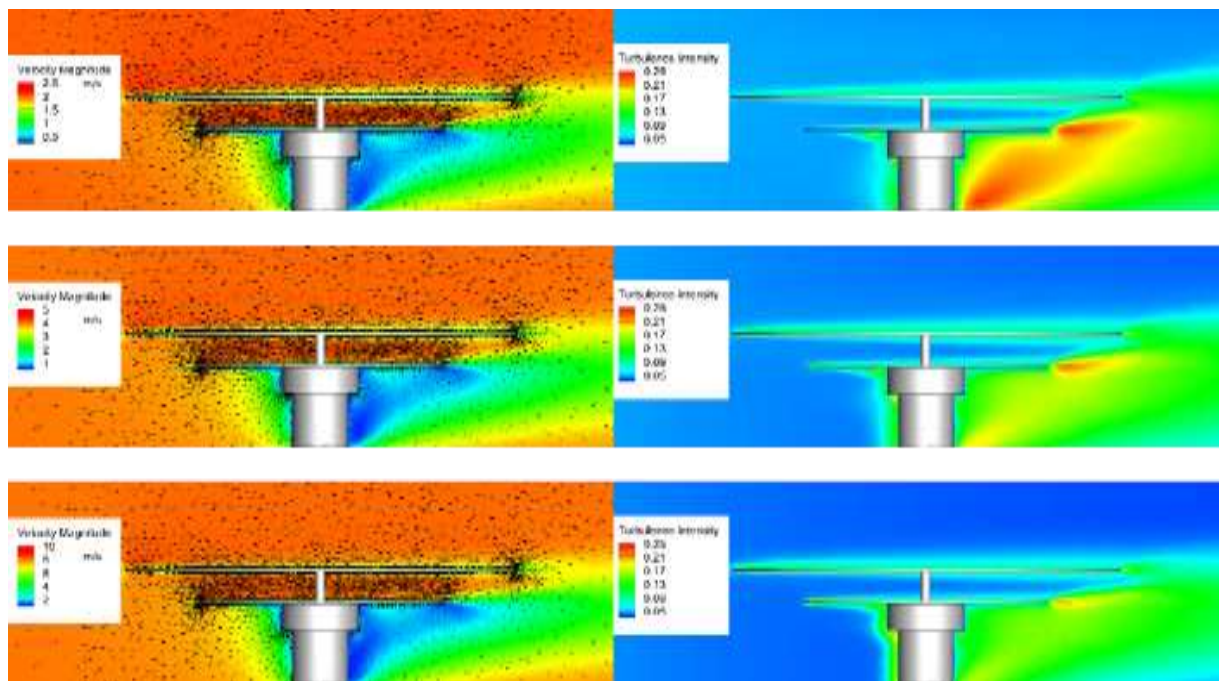
Figure 4: Flat plate Sampler: Velocity magnitude and turbulence intensity at wind speed 2 m/s (top), Flat plate Sampler: Velocity magnitude and turbulence intensity at wind speed 4 m/s (middle), Flat plate Sampler: Velocity magnitude and turbulence intensity at wind speed 8 m/s (bottom).

3.2.1   Sigma 2 Sampler

The cross section of the velocities for the Sigma-2 are shown for the 4 m/s case in **Figure S 27**. Apparently the velocity magnitude inside the sampler is much smaller than outside. In the vertical settling tube, the turbulence intensity is low, justifying the idea of Stokes settling inside. Owing to the open, but bulky geometry, there is a flow into the interior at the back. The highest velocities and turbulence intensities are found at the sharp edges at the top and bottom of the sampler.

Figure S 28 shows the cross section of the velocities for the MWAC in the 4 m/s case. Furthermore, the velocity field and the velocity vectors in the cross sections across and along the inlet tube are shown in

Figure S 29. In the tubes the typical pipe flow is formed. In the figures showing the cross sections along the inlet tube a symmetrical flow over the pipe cross section is visible. Finally, **Figure S 30** shows the mean flow velocity in the MWAC tube is shown as a function of the outside velocity for the three cases. The fitting curve shows that the mean velocity in the pipe increases linearly with the external velocity.

4   Results and Discussion

4.1   Methodical aspects (Field Measurements)

4.1.1   Mass deposition rate comparison

Mineral dust was the dominating particle type during this campaign, consisting of different silicates, quartz, calcite, dolomite, gypsum, similar to previous findings for this location (Kandler et al., 2007). Therefore, hygroscopicity was not taken into account, as due to the mostly non-hygroscopic compounds and the moderate humidities their impact was rated low. Details on the composition will be reported in a companion paper.

The mass and number deposition rates (given per unit time and sample surface area) along with daily average temperature and wind speed are presented as daily values. Details for all days and all samplers can be found in the electronic supplement (see **Table S 1, S 2, S 3** and **S 4**). All data shown in this section are calculated from SEM measurements. Particle sizes are reported as aerodynamic diameter, if not otherwise stated. It is also worth mentioning the plots shown in the paper are a few examples of a comparison while the bulk of the data is presented in the electronic supplement.

Figure 5 shows as example mass deposition rates for different samplers during a dust event and a non-dust event day. For all samplers, the mass deposition rate size distributions peaked in the 8-16 μm diameter interval. This result is in support of the conclusion that atmospheric dry deposition is dominated by coarse particles owing to their high deposition velocities (Davidson et al., 1985; Holsen et al., 1991). There is a considerable difference among different samplers affecting mainly the size range with the highest mass deposition rates, whereas the difference is small for smaller particles. MWAC and BSNE – both horizontal flux samplers – collect coarser material than the Flat plate and Sigma-2 samplers, which in contrary measure the vertical flux. In particular, the MWAC sampler exhibits considerably higher coarse particle mass deposition rates, probably owing to its impactor-like design.

429

430

Table 2: The campaign maximum and minimum and median mass deposition rates measured by the samplers

Sampler	Maximum deposition rate (mg/ (m^{2}d))	Minimum deposition rate (mg/ (m^{2}d))	Median deposition rate (mg/ (m^{2}d))
MWAC	1240	0.6	4.8
BSNE	310	0.2	3.1
Flat plate	80	2.0	1.1
Sigma-2	117	1.9	1.1

433

As consequence the vertical flux instruments collect much less material than the horizontal flux ones (**Table 2**), which is in accordance with previous findings (Goossens, 2008). In the present study, horizontal to vertical flux mass ratio is approximately between 2.8 and 4.4 (with single size intervals ranging between 2 and 50), while Goossens (2008) reported it to be in between 50 and 160. This difference in the ratio might come from the different approaches. Goossens (2008) used water as a deposition surface while in our study we used a SEM sampling substrate. Furthermore, from **Figure 5**, we can clearly see that that there is a strong variation in mass deposition rates between dust event days and non-dust event days (full dataset is shown in **Figure 6**). Generally, the temporal variation is higher than the difference between the samplers so a strict comparison between this and the previous study can't be done.

444
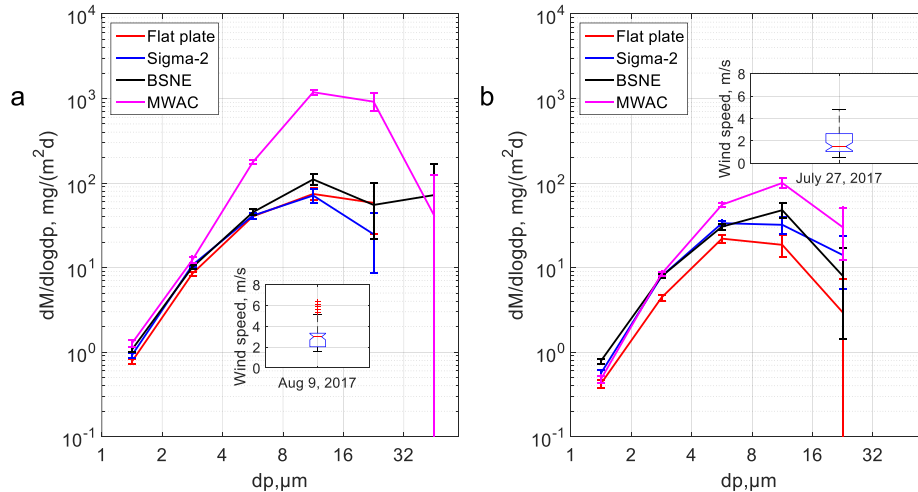
Figure 5: Size resolved mass deposition rate measured by different passive samplers: a) dust event day; b) non-dust event day. Data are derived from SEM measurements. The bars show the central 95% confidence interval of the daily variation. The inserts show box plots for the wind speed distribution based on 30-min intervals.

449
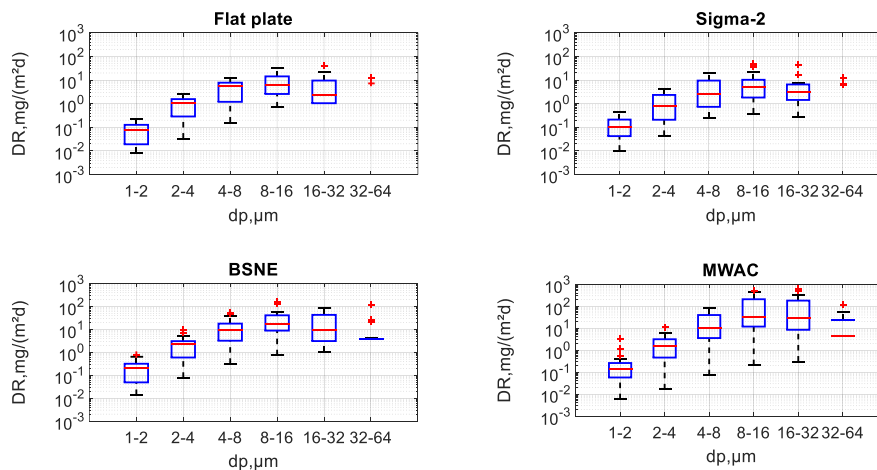
Figure 6: Box-plots of size resolved deposition rate (campaign data; Flat plate, Sigma-2, MWAC and BSNE samplers). On each blue box, the central mark is the median, the edges of the box are the 25th and 75th percentiles. The red vertical lines show the standard deviation. The median, percentiles and standard deviations shown there correspond to the variability of the whole campaign for each

454 instrument and bin. From the structure of the deposition models, a wind speed dependency for the

455 deposition velocity should be expected. The average wind speed during the campaign was about 3.5

456 m/s with the lowest daily median around 1.5 m/s and the highest 7 m/s. A daily box-plot of 30-min

457 averaged wind speed at Izaña is shown in **Figure S 1**.

458 **Figure 7** shows the mass deposition rate ratio of MWAC, BSNE and Flat plate to Sigma-2 as function

459 of wind speed. The Sigma-2 sampler was chosen for comparison, as due to its settling tube design, it is

460 expected to have the least wind sensitivity. The results show highly scattered values. The collection

461 efficiency of MWAC for large particles has an increasing tendency in comparison to Sigma-2 slightly

462 with increasing wind speed, while there is barely a trend visible for the BSNE. Both – being horizontal

463 flux samplers – collect considerably more material than the Sigma-2. For the Flat plate, the deposition

464 velocity in relation to the Sigma-2 has a weak decreasing trend for higher wind speeds, but generally, the

465 deposition speed is similar. Overall, the relation of Sigma-2 to BSNE shows the closest agreement, while

466 the scatter is higher for the other combinations. More information on the relation between the other

467 instruments is shown in **Figure S 2, S 3, S 4, S 5, S 6, S 7, S 8, S 9** and **S 10**.
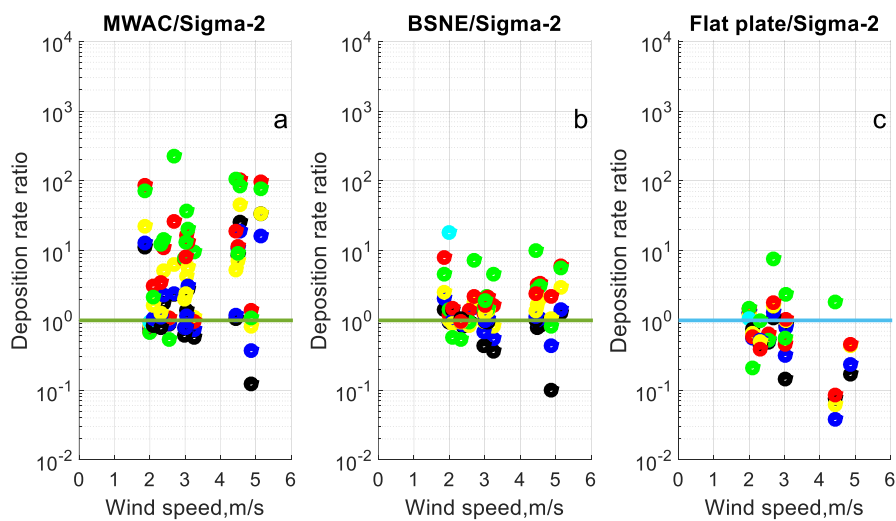
468

469 **Figure 7**: Deposition rate ratio as function of wind speed for different days (MWAC/ Sigma-2 (a),

470 BSNE/Sigma-2 (b) and BSNE/ Sigma-2 (c)). Different colors represent deposition rate measured in

471 different size intervals (black: 1-2 µm; blue: 2-4 µm; yellow: 4-8 µm; red: 8-16 µm; green: 16-32 µm;

472 cyan: 32-64 µm).

473 While without a true reference technique the absolute deposition velocities can't be determined, their

474 ratio between different instruments can be compared theoretically and by measurement. The deposition

475   velocity ratios for a pair of different samplers are identical to the deposition rate ratios obtained from the

476   corresponding measurements (eq. (7)), as long as the sampling time and the aerosol concentration are the

477   same; the latter condition is achieved by the close and parallel sampling. Therefore, the experimentally

478   determined ratios can now be compared to the deposition velocity ratios derived from the theoretical

479   considerations. **Figure 8** shows the according comparison. Note that this consideration allows for the

480   assessment of relative model performance and sampler efficiency, but lacking a 'true' reference, it does

481   not allow for determining the most accurate sampler.

482   While for BSNE and Sigma-2 observation and model fit comparatively well, the deposition velocity is

483   misestimated for the Flat plate/Sigma-2 pairing for all particle sizes (overestimate for Flat plate

484   deposition velocity or/and underestimate for Sigma-2). For MWAC/Sigma-2, there is a clear size

485   dependency, indicating that probably the impactor model overestimates the deposition velocity; the latter

486   might be due to unaccounted particle losses (e.g., inlet efficiency). MWAC, BSNE and Sigma-2 agree

487   with respect to deposition velocity better based on the measurement data than predicted by the theory. It

488   may be connected to the non-stationarity of the atmosphere, which is not accounted for by the models,

489   i.e. the permanent wind speed fluctuations smoothing out detail differences of a stationary flow. The Flat

490   plate sampler, however, has a lower-than-predicted deposition velocity.
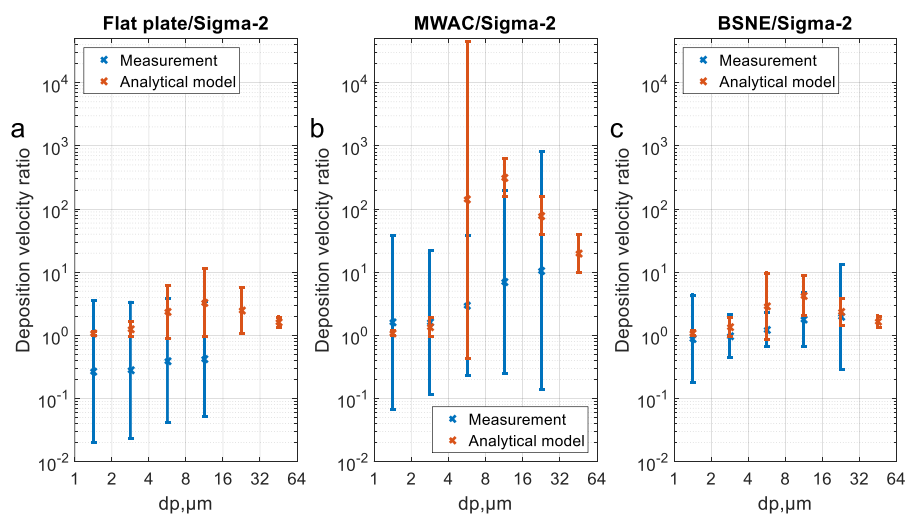
491

492   **Figure 8**: Comparison of geometric mean ratio of deposition velocities for different sampler pairs

493   derived from measured deposition rates (blue) and from corresponding deposition models (orange).

(a) Flat plate/Sigma-2; (b) MWAC/Sigma-2; (c) BSNE/Sigma-2. Error bars show geometric standard deviations. The bars show the central 95% confidence interval of the daily variation. According deposition models are listed in **Table 1**.

4.1.2 Dependence of PM_{10} dust deposition on atmospheric concentration and wind speed

Figure S 22 and **Table 3** display for the approximate PM_{10} size range the correlation between number deposition rates, atmospheric particle number concentrations measured by OPC and the wind speed for different samples. For this consideration, only the overlapping size range – 1-10 μm aerodynamic diameter – was used. As expected, there is in all cases a positive correlation between concentrations and number deposition rates (see **Figure S 22a)**. In particular, for the BSNE and the Simga-2, robust correlations with a trend to underestimation at higher concentrations exist. While the models predict a positive correlation of wind speed and deposition rate, this is not observed in the measurements. E.g., the table does not show a linear correlation since the r^2 values are not close to 1 for the first two samplers (particularly the MWAC). Instead, a non-significant anti-correlation can be observed, if at all (e.g., for Flat plate; r²: 0.319, p-value = 0.070, slope=-0.261) (see **Figure S 22b**), indicating a cross-influence of wind speed and concentration. E.g. higher concentrations of dust aerosol particles might be meteorologically linked to lower wind speeds due to a different transport situation. Such a general behavior was observed previously for example by different techniques for a dust transport region (Kandler et al., 2011). An ambiguous wind-dependency has been reported for other places (Xu et al., 2016). In this study, the main driver of the deposition rate during is obviously the dust concentration.

Table 3: Summary of the regression analysis for the correlations between the dust deposition rate and the atmospheric concentrations (**PM_{10}** size range; measured by the OPC), and for the correlations between the dust deposition rates and the wind speeds. Significant relationships are shown in bold.

	Deposition rate vs concentration			Deposition rate vs wind speed		
	r²	p-value	slope (m/d)	r²	p-value	Slope ($1.16*10^5$ /(m^3))
Flat plate	0.600	0.0052	0.492	0.319	0.070	-0.261
MWAC	0.155	0.335	0.146	0.308	0.153	-0.157
BSNE	**0.937**	**$1.00*10^{-6}$**	**0.832**	0.017	0.706	-0.052
Sigma-2	**0.925**	**$3.39*10^{-5}$**	**0.725**	0.0125	0.775	-0.069

In a second step is was tested, whether the application of each sampler's assigned deposition model can increase the correlation between the measurements by the deposition samplers and the OPC observations, i.e. whether the meteorological parameters accounted for in the models can decrease the deviation. Therefore, in analogy to the previous correlation, the concentrations modeled from each sampler's SEM data were correlated with the OPC data for the size range between 1 and 10 µm in particle diameter (see **Table S 7**). However, no increase in correlation quality is observed, indicating that – like already observed from the varying ratio calculations above – the deposition models fail to describe the deposition behavior in detail.

From the correlation relations in **Table 3**, it can be learned that MWAC is least suitable for estimating PM_{10}, which fully agrees well with previous studies (Mendez et al., 2016). However, the correlation analysis here shows that BSNE is actually a suitable instrument for a PM_{10} estimation, which is in contrast to the wind-tunnel observation of Mendez et al. (2016). This discrepancy might be owed to the different approaches. While in the previous work the loss of concentration from the passing aerosol was measured, in this study a gain of deposition was investigated. As result, for lower deposition velocities (discussed below), the former approach will yield high uncertainties. Similar to BSNE, Flat plate and Sigma-2 appear good estimators for PM_{10}, which is in accordance with previous studies (Dietze et al., 2006).

4.1.2.1 Size-resolved apparent deposition velocity in the PM_{10} size range

Figure 9 displays the apparent deposition velocity (calculated as the ratio of the number deposition rate to the concentration of the OPC) as function of the wind speed. Obviously, also here there is not clear trend. The apparent deposition velocities range between $2*10^{-4}$-10^{-1} m/s. As can be clearly seen from the plot, the effect of wind speed on deposition velocity is negligible, as indicated already in **Table 3**. While this is in contradiction to the models, one has to keep in mind that the (a) the observed wind speeds are comparatively low here, and (b) the considered size range is not the one most affected by the wind speed. An effect of the wind speed might therefore be much stronger at higher wind speeds and for larger particles.

542
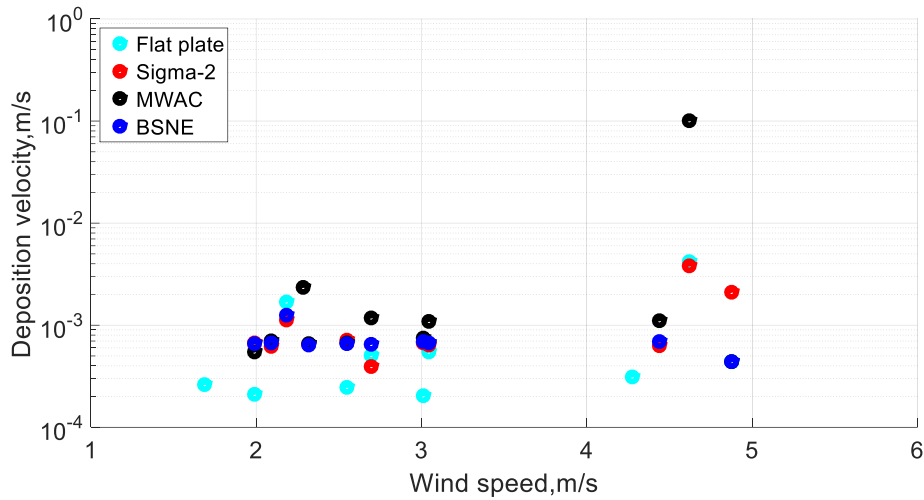
Figure 9: Apparent deposition velocity: ratio of number deposition rate determined from SEM
measurements to the number concentration observed by the OPC as function of wind speed. For the
consideration, only the overlapping size range (approximately 1-10 μm) was used.

543
544
545

546   4.1.3   Atmospheric mass concentrations derived from deposition rates

547   4.1.3.1   Consistency between samplers and corresponding models

548   **Figure 10** compares a mass deposition rate size distribution with the according concentrations derived
549   by the modeled deposition velocities. Calculating the mass concentrations from different passive
550   samplers with different models leads in most cases to a better agreement between the measurements,
551   taking into account the statistical uncertainties (see **Figure S 11**). This indicates that the deposition
552   velocity models selected for the samplers are generally suitable, despite the deviations in single cases.

553

554
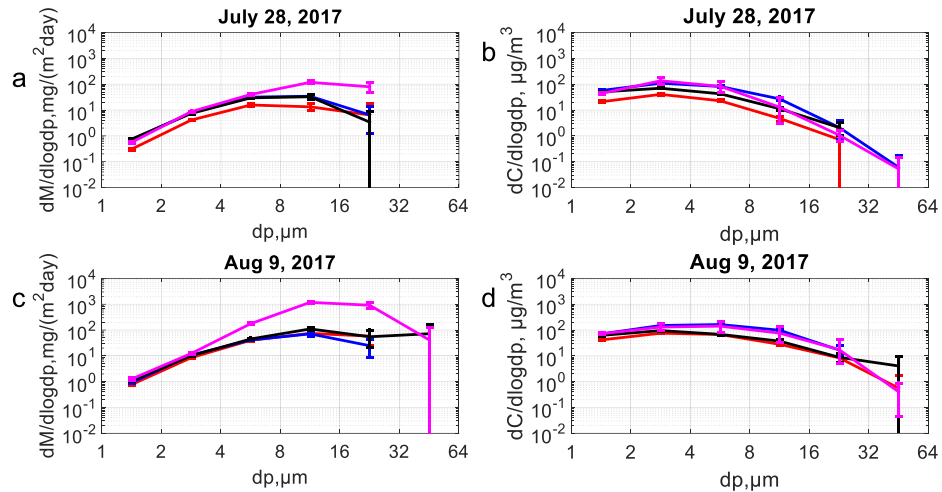
Figure 10: Comparing different samplers with respect to (a, c) dust mass deposition rates and (b, d) dust mass concentrations calculated from application of the corresponding model as function of particle size. Different colors indicate different samplers (red: Flat plate; blue: Sigma-2; black: BSNE and magenta: MWAC). The bars show the central 95% confidence interval of the daily variation. According deposition models for concentration calculation are given in the **Table 1**.

4.1.3.2   Size-resolved comparison with active samplers

The calculated number concentrations in the size interval between 1–10 μm are compared with the concentrations measured using the OPC. Similarly, the mass concentration size distributions above the PM$_{10}$ size range are validated using the FWI measurements.

Figure 11 (see also **Figure S 14, S 15, S 16** and **S 17**) shows a comparison of number concentration size distributions calculated from deposition rate measurements of the Flat plate, Sigma-2, BSNE and MWAC samplers with the number size distributions measured by the OPC for different days. Overall, most of the times the number concentrations obtained from OPC measurements are slightly higher than the ones from the deposition rates for the size range 2-5 μm and for dust days, with the exception of the Sigma-2, when considering only Stokes' velocity. This reflects the tendency of a relative underestimation of the concentrations by the passive techniques for high concentrations, which was already visible in the correlation analysis above. In general, **Figure 11** shows that the deviation of calculated values from OPC measured values is significant.

In this context, **Figure 11** shows also the low influence of the two techniques used for u_* estimation. While the number concentrations derived using the friction velocity estimated from Wood (1981)

575   formulation are slightly higher and therefore in better agreement with the OPC data, the difference

576   appears to be negligible in general, probably owing to the relatively low wind speeds in this study.
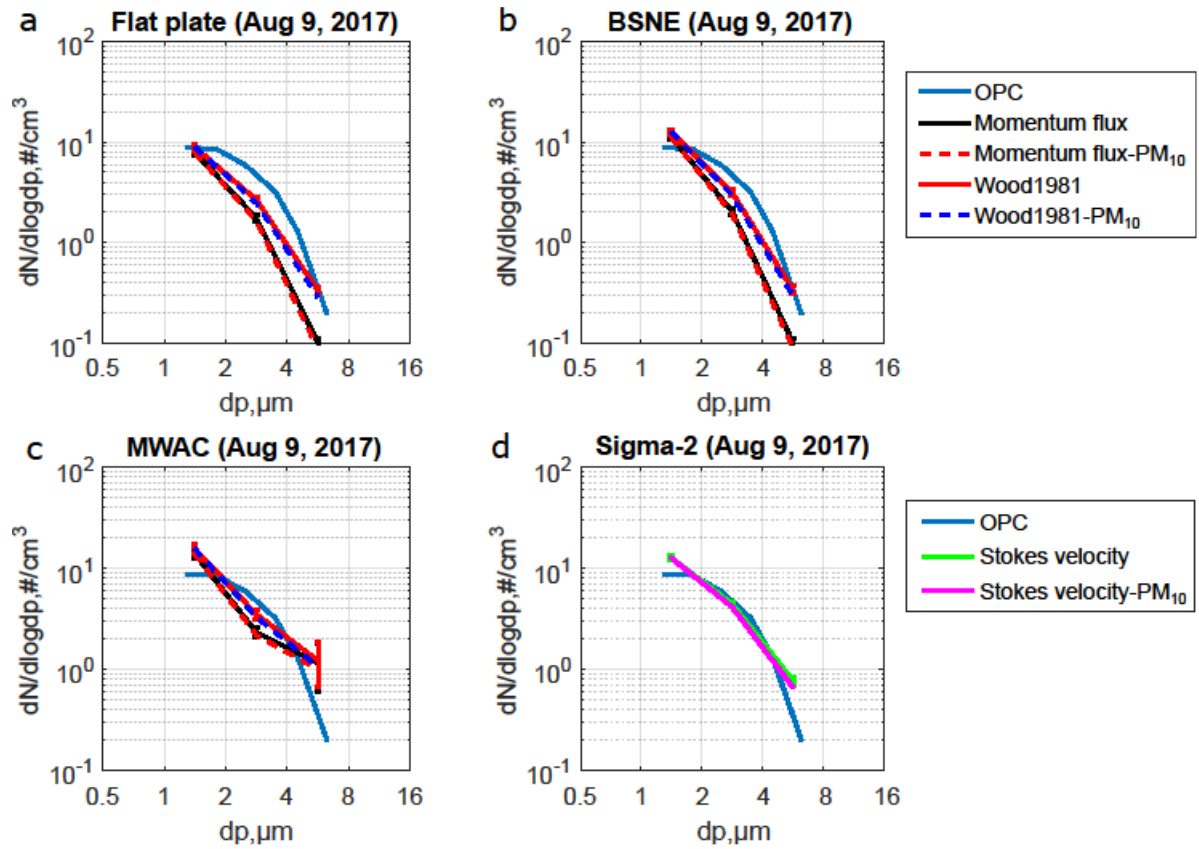
Figure 11: Comparison of the number concentrations calculated from the deposition measurements
with the number concentrations measured by the OPC. Number size distributions are obtained by
converting the SEM number deposition rates to number concentrations using the different deposition
velocity models (**Table 1**), in analogy to the mass size distributions. For the concentrations obtained
from the number deposition rates, two different approaches for the friction velocity are shown. The
black curve shows the concentration curve calculated using the momentum flux approach without PM_{10}
inlet correction (i.e. the atmospheric concentration). The red curve shows the concentration curve
calculated using the Wood approach without PM_{10} correction. The dotted blue curve shows the
concentration curve calculated using the Wood approach with PM_{10} inlet correction (simulating the
concentration the OPC would supposedly measure). The dotted red curve shows the concentration
curve calculated using the Momentum flux approach with PM_{10} inlet correction. In case of the Sigma-2,
the green curve shows the concentrations calculated using the Stokes velocity and the magenta curve
the ones using Stokes velocity with the PM_{10} inlet correction. The bars show the central 95%
confidence interval of the daily variation. (a): Flat plate; (b) BSNE; (c): MWAC; (d) Sigma-2. The
average wind speed on Aug 9, 2017 was 3.0 m/s. Note that panel (d) refers to the second legend.

Figure 12 (see also Figure S 12) shows the comparisons for the larger particles between the deposition-derived number concentrations and the ones from the FWI. Here, a significant inconsistency occurs between the mass size distributions from passive samplers and the ones from FWI. In particular, the size range larger than 10 µm seems to be generally underestimated by the passive samplers. While for particles around 10 µm, this could be partly to a badly-defined collection efficiency curve of the FWI ((Kandler et al., 2018); 50 % cut-off at 11 µm) and the according correction, this can't be the reason for the particles larger than 16 µm, where this efficiency approaches unity. Here, the deposition velocity for the samplers is apparently overestimated. A possible explanation would be inlet losses of the passive sampler, but this need to be subject of further research. An overview of the OPC measurements comparing the size distributions between the long-term (deposition) and short-term (FWI) sampling is shown in Figure S 13.
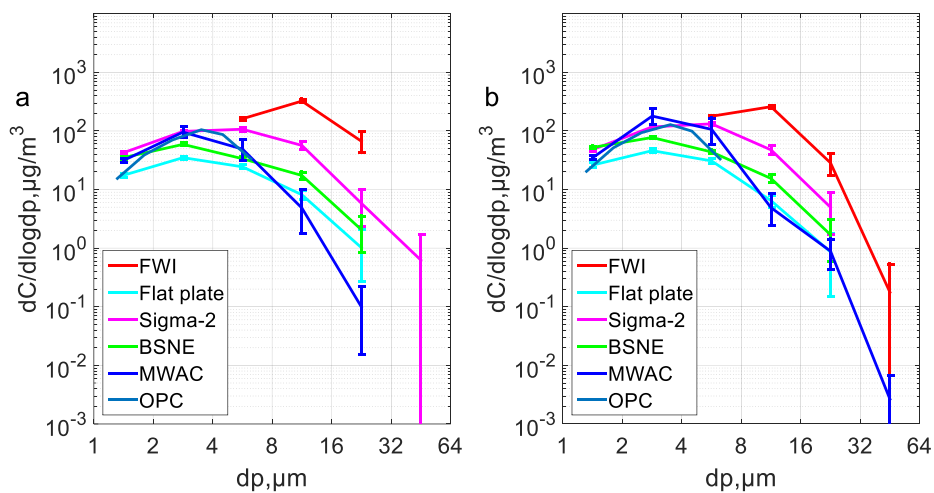
Figure 12: Daily average mass size distributions obtained from the passive sampler techniques in comparison to an active sampler (FWI). Mass concentration size distributions were calculated from the SEM mass flux measurements using the corresponding deposition velocity models. Samples were collected on 26th of July (a) and 27th of July (b). The mass concentration measurements shown by the FWI are daily averages (3 samples per day). The bars show the central 95% confidence interval of the daily variation.

In a last step, the deposition-derived concentrations are compared to these determined from the iso-axial filter sampler. Figure 13 shows that, while the calculated size distributions are in good agreement with

the OPC ones, the filter-derived seem to relatively underestimate the concentrations. A correlation analysis (R-squared: 0.681, p-value = 0.0854 and slope = 2.0394) suggests, that there is a weak positive correlation between calculated number concentration from filter samples and the OPC measured concentration. BSNE has been chosen here for comparison, as its agreement with the OPC measurements is generally the closest. The reasons for this weak correlation between the filter sampler and the OPC measurements – in particular compared to the stronger correlation between Sigma-2 and BSNE with the OPC – are not clear. For sake of completeness, the same comparison for the other samplers is shown in **Figure S 18, S 19** and **S 20**. While in general here, the disagreement between the Filter sampler and the MWAC and Sigma-2 samplers is significant, for the Flat plate sampler less disagreement occurs. In addition, an overview of the OPC measurements comparing the size distributions between the long-term (deposition) and short-term (filter) sampling is shown in **Figure S 21**.
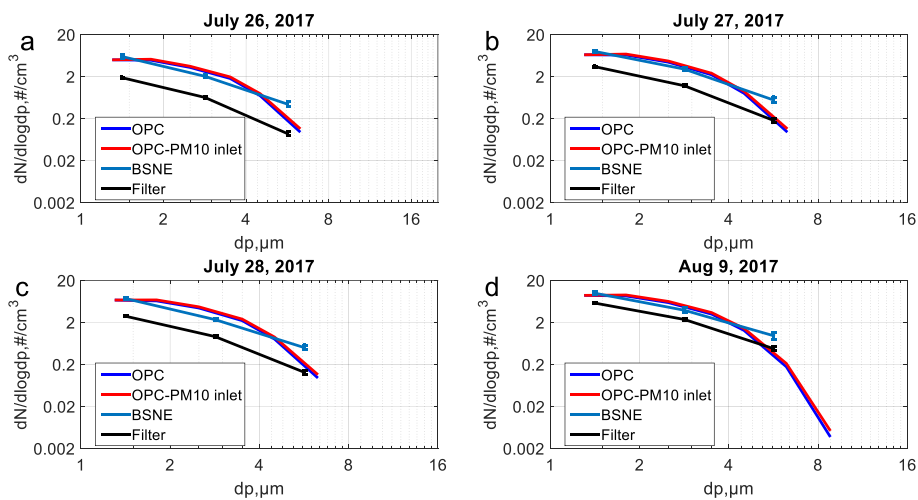
Figure 13: Average size distributions obtained from the SEM analysis of the filter sampler, in comparison to BSNE and OPC for different measurement days (a: July 26, 2017; b: July 27, 2017; c: July 28, 2017; d: July 29, 2017). Number concentration size distributions from deposition are obtained by converting the SEM obtained number deposition rates to number concentration using different deposition velocity models. The red curve shows the OPC with PM_{10} inlet efficiency correction (representing the atmospheric concentration). The number concentration measurements shown for the filter sampler are daily averages. The bars show the central 95% confidence interval of the daily variation.

4.1.4 Estimating the turbulent versus gravitational transport fraction

The size-resolved upward and downward deposition rates were derived from the upward-/downward facing deposition sampler by the same type of SEM analyses. Results of the size resolved-mass and number deposition rate measurements along with daily average temperatures and wind speeds are given in the electronic supplement (see **table S 5** and **S 6**). The upward deposition rate is always less than the downward deposition rate. This is expected because the upward facing substrate (i.e. measuring the downward-directed deposition rate) collects particles deposited by gravitational settling and turbulent inertial impaction, while the downward facing substrate (for the upward-directed deposition rate) collects particles only by means of turbulent impaction. **Figure 14** shows the ratio of upward to downward mass deposition rate as function of particle size. The deviation is greatest for the particle size range around 8 μm, which is strongly affected by turbulence (Noll and Fang, 1989). However, nearly no trend of increasing ratio with increasing wind speed can be found here (see **Figure S 23**). Besides the wind speed magnitude, different properties were calculated from the sonic wind data (e.g., turbulent intensity, Monin-Obukhov length, relative standard deviation of wind speed, average vertical component), but none of them was able to explain the observed variations in the deposition rate ratio.
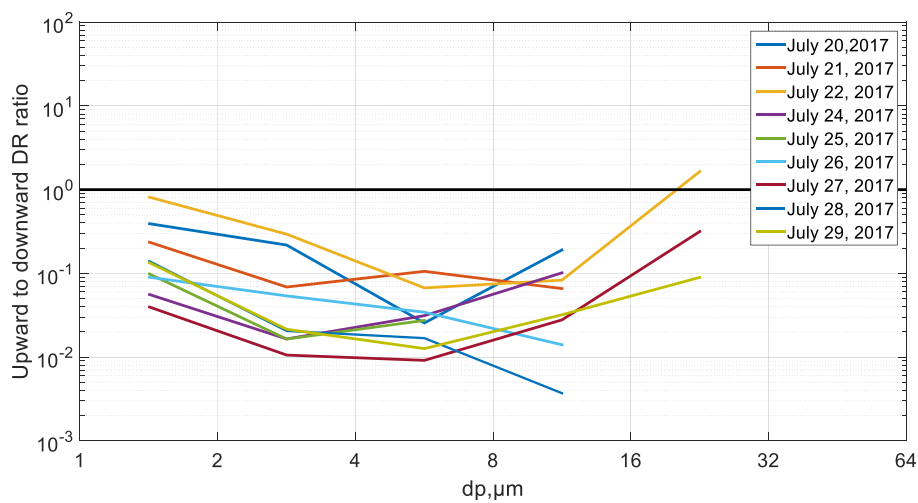
Figure 14: Ratio of upward- to downward-directed mass deposition rate as function of particle size. The deposition rate is measured using the upward-downward-Flat plate sampler (with 25 mm stub).

4.2 Computational fluid dynamics (CFD) simulation

Using computational fluid dynamics (CFD), deposition velocities of particles for different passive samplers were predicted and compared to the analytical deposition velocity models used for the different samplers (see **Figure 15** and **Figure S 31**). While for the Flat plate and MWAC sampler the curves agree qualitatively (i.e. showing deposition speeds higher than Stokes velocity at particles sizes 4-16 μm, which are supposedly strongest affected by turbulence), for the Sigma-2, they are largely contrary except for the lowest wind velocity. The latter might be owed to the fact that in a flow model, the non-omnidirectional construction of the Sigma-2 might lead to preferred airflows, which are not relevant in a more variable and turbulent atmosphere. However, also for the former ones, the deposition velocity curves are quantitatively largely different. In this context, **Figure S 32** shows a comparison of the CFD-derived particle deposition velocities at different wind speed values for different samplers. For the Flat plate and the MWAC samplers, the deposition velocity increases with the wind speed, while for the Sigma-2 sampler, such a relation is not observed. Moreover, it can be seen from the figure that in general for the Flat plate and the MWAC samplers, Stokes' velocity is considerably lower than the deposition velocities calculated at different wind speeds by the other models. Interestingly, however, this is not true in the case of Sigma-2 sampler. In general, for the effect of wind speed on the Sigma-2 sampler is not yet clear, why there is an effect for some sizes and for others not, so further modeling work is needed.
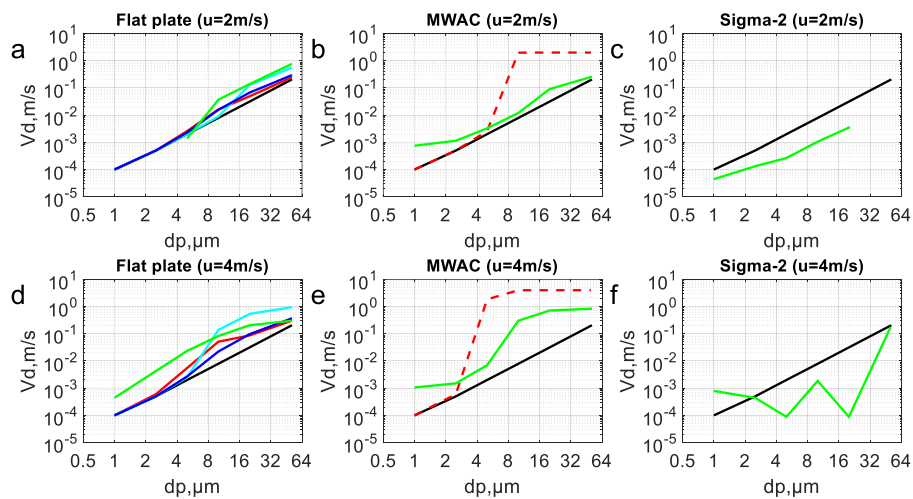
Figure 15: Deposition velocities calculated for different samplers by analytical and CFD approaches. The red curve shows the deposition velocity calculated using the Piskunov model, the dotted red curve shows the combination of the Piskunov and the impaction curve model, the black curve shows the Stokes deposition velocity, the blue curve the Noll and Fang model, the cyan the Zhang model, and the

675   green curve finally the deposition velocity from CFD. Panels **a-c** are calculated for 2 m/s wind speed,

676   **d-f** for 4 m/s.

4.3   Comparison of measured deposition rate ratios to analytically and CFD modeled ones

678 As there is no reference instrument for dry deposition sampling, the separate approaches are compared

679 in a relative way. **Figure 16 a-c** show comparisons of the deposition velocity ratios derived from the

680 analytical models with the according measured deposition velocity ratios (equalling the according

681 deposition rate ratios), **d-f** the respective correlation of the ratios derived from CFD modeling with the

682 measurement. As the CFD models could only be calculated for a limited number of flow velocities,

683 deposition velocity values were interpolated between the calculated cases. Generally, the agreement is

684 very poor. Practically, no variation observed in the measurement data can be explained by model

685 variation, independently of the type of model. While this might be explained to a smaller extent by the

686 propagating measurement uncertainties for the largest particles with low counting statistics, for the

687 smaller ones this systematic deviation must have other reasons.

688
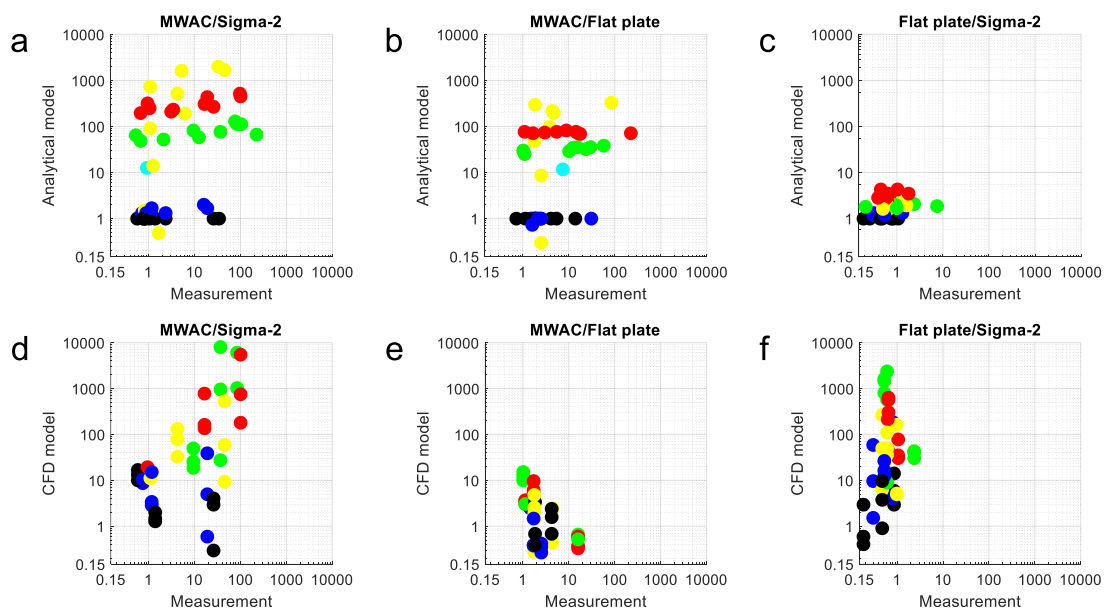
689 **Figure 16**: Comparison of the observed deposition velocity ratios with modeled ones by the analytical

690   deposition models (upper row, a-c) and by the CFD models (lower row, d-f). (a, d) MWAC/Sigma-2;

691 (b, e) MWAC/Flat plate; (c, f) Flat plate/Sigma-2. Multiple daily measurements are shown in each plot.

692 Different colors represent different size intervals. 1-2 µm: Black, 2-4 µm: Blue, 4-8 µm: Yellow, 8-16

693   µm: Red, 16-32 µm: Green, 32-64 µm: Cyan.

5 Summary and Conclusions

Parallel dust aerosol deposition measurements by means of deposition and other passive samplers were conducted at Izaña Global Atmospheric Watch observatory continuously from 14th of July to 24th of August 2017. In addition, active aerosol collection was done with a free-wing impactor and an iso-axial filter sampler. Additional information regarding the aerosol particle size distributions has been obtained by an OPC. 316,000 single particles from 6 different samplers were analyzed by SEM-EDX, yielding size resolved deposition rates.

As known from previous studies, the total deposition rate was dominated by coarse particles (8-16 μm). A high temporal daily variability in total dust deposition rate was observed. The size resolved deposition rate measurements of different passive samplers varied significantly between the samplers under the same conditions. This was in principle expected from the different sampler construction. Applying suitable deposition velocity models, atmospheric concentrations were calculated from different sampler deposition rates. The resulting concentrations on average are in better agreement between the samplers than the deposition rates. However, discrepancies beyond the measurement uncertainty remain unexplained by the deposition models, in particular with respect to dependency on wind speed, which is predicted by the models, but not observed. The estimation of an appropriate deposition velocity from different models for calculating atmospheric concentrations remains obviously a challenge. In particular, when considering the size-resolved deposition velocities and deposition rate ratios, great discrepancies show up. While for an integrated bulk measurement or the PM_{10} size range at least a qualitative agreement between the samplers can be reached, no model – analytical nor CFD – is able to explain the observed sampler-specific variations in deposition rate. Clearly, a better physical understanding is needed here.

In the PM_{10} size range, a good agreement is found between the calculated concentrations for samples from different passive and the concentrations measured using an OPC. For particle sizes above PM_{10}, the comparison of the deposition-derived size distributions with impactor and filter measurements shows considerable underestimates of the deposition samplers, which must be interpreted as overestimation of the large-particle deposition velocities.

Deposition velocities from different analytical deposition models are compared to ones calculated using computational fluid dynamics simulations for different samplers. The comparison shows that two methods largely disagree. Moreover, all theory-based deposition velocities (analytical as well as CFD approaches) fail to represent the observed measurement differences between the samplers. This obviously points to the need of better understanding the physics of dry deposition in general.

The correlation analysis between dust deposition rate, dust concentrations and wind speed reveals that the variation in deposition rate is mainly controlled by changes in concentration; variations in wind speed play a minor role for wind speeds lower than 6 m/s. However, the situation might be different for higher wind speeds (Kandler et al., 2018).

The correlation analysis between deposition rates and OPC measurements demonstrated that BSNE and Sigma-2 can be a good option for PM_{10} measurement, while the MWAC is not a suitable option. Apart from that result with respect to the PM_{10} size range, no recommendation for a least biased general purpose deposition sampler can be derived from our study.

Moreover, as the results show that the different samplers can't deliver consistent results between the sampler types, a recommendation must be that if a certain sampler type is chosen for a study, it should not be modified or replaced by another one for sake of consistency of results, even if it was shown that the results do not agree well for example with active sampling. The results show, nevertheless, that passive sampling techniques coupled with an automated single particle analysis provides insights into the variation of size distribution, deposition rate and concentration of atmospheric particles.

6 Acknowledgements

This project is funded by the Deutsche Forschungsgemeinschaft (DFG, German Research Foundation) – 264907654; 264912134; 416816480 (KA 2280). We would like to thank for the financial support by the DFG in the framework of the Excellence Initiative, Darmstadt Graduate School of Excellence Energy Science and Engineering (GSC 1070). We thank our colleagues Thomas Dirsch and Conrad Ballschmiede. We are grateful to all staff members of Izaña Global Atmospheric Watch Observatory for helping us in maintenance of the sampling equipment. We are especially indepted to Dr Roger Funk from Leibniz-Centre for Agricultural Landscape Research, Institute of Soil Landscape Research for providing us some of the passive samplers.

7 Author contribution

A. W. conducted the field measurements and did data evaluation and interpretation. K. S. helped with the field measurements, carried out the SEM analyses and did data processing. J. M. and B. E. executed the CFD model setup and calculations. S. R. operated the OPC including the data processing and the meteorological base measurements. K. K. designed the experiment, designed and prepared the sampling equipment and did data processing and interpretation. All authors contributed to the data discussion and manuscript preparation.

8   Data availability

The data sets used for this publication are available from the Pangaea repository free of charge (https://doi.pangaea.de/10.1594/PANGAEA.901413)

References

Aluko, O. and Noll, K. E.: Deposition and suspension of large, airborne particles, Aerosol Sci. Technol. , 40, 503-513, 2006.

Andreae, M. O.: Climatic effects of changing atmospheric aerosol levels, in: Future Climates of the World, World Survey of Climatology Henderson-Sellers, A. (Ed.), Elsevier, New York, 1995.

Arimoto, R.: Eolian dust and climate: relationships to sources, tropospheric chemistry, transport and deposition, Earth Sci Rev. , 54, 29-42, 2001.

Arya, S.: Suggested revisions to certain boundary layer parameterization schemes used in atmospheric circulation models, Mon Weather Rev., 105, 215-227, 1977.

Belyaev, S. and Levin, L.: Techniques for collection of representative aerosol samples, J. Aerosol Sci., 5, 325-338, 1974.

Bergamaschi, P., Bräunlich, M., Marik, T., and Brenninkmeijer, C. A.: Measurements of the carbon and hydrogen isotopes of atmospheric methane at Izaña, Tenerife: Seasonal cycles and synoptic-scale variations, J Geophys Res Atmos., 105, 14531-14546, 2000.

Chmielewski, M. and Gieras, M.: Three-zonal wall function for k-ε turbulence models, CMST, 19, 107-114, 2013.

Davidson, C. I., Lindberg, S. E., Schmidt, J. A., Cartwright, L. G., and Landis, L. R.: Dry deposition of sulfate onto surrogate surfaces, J Geophys Res Atmos., 90, 2123-2130, 1985.

Davies, C.: Particle-fluid interaction, J. Aerosol Sci 10, 477-513, 1979.

Dietze, V., Fricker, M., Goltzsche, M., and Schultz, E.: Air quality measurement in German health resorts-Part 1: Methodology and verification, Gefahrstoffe-Reinhalt. Luft. , 66, 45-53, 2006.

Dupont, S., Rajot, J. L., Labiadh, M., Bergametti, G., Alfaro, S., Bouet, C., Fernandes, R., Khalfallah, B., Lamaud, E., and Marticorena, B.: Aerodynamic Parameters Over an Eroding Bare Surface: Reconciliation of the Law of the Wall and Eddy Covariance Determinations, J. Geophys. Res. Atmos. , 123, 4490-4508, 2018.

783   Efron, B.: Bootstrap Methods: Another Look at the Jackknife, Ann. Statist., 7, 1-26, 1979.

784   Einstein, S. A., Yu, C.-H., Mainelis, G., Chen, L. C., Weisel, C. P., and Lioy, P. J.: Design and validation
785   of a passive deposition sampler, J. Environ. Monit., 14, 2411-2420, 2012.

786   Ettling, D.: Theoretische Meteorologie, Vieweg, Braunschweig/Wiesbaden, 1996. 1996.

787   Fluent, A.: Theory guide, Ansys Inc, 2015. 2015.

788   Fryrear, D.: A field dust sampler, J. Soil Water Conserv., 41, 117-120, 1986.

789   García, R., García, O., Cuevas, E., Cachorro, V., Barreto, A., Guirado-Fuentes, C., Kouremeti, N.,
790   Bustos, J., Romero-Campos, P., and de Frutos, A.: Aerosol optical depth retrievals at the Izaña
791   Atmospheric Observatory from 1941 to 2013 by using artificial neural networks, Atmos. Meas. Tech. ,
792   9, 53-62, 2016.

793   Giardina, M. and Buffa, P.: A new approach for modeling dry deposition velocity of particles, Atmos.
794   Environ., 180, 11-22, 2018.

795   Goossens, D.: Relationships between horizontal transport flux and vertical deposition flux during dry
796   deposition of atmospheric dust particles, J. Geophys. Res., 113, 2008.

797   Goossens, D. and Buck, B. J.: Can BSNE (Big Spring Number Eight) samplers be used to measure PM10,
798   respirable dust, PM2. 5 and PM1. 0?, Aeolian Res. , 5, 43-49, 2012.

799   Goossens, D. and Offer, Z. Y.: Wind tunnel and field calibration of six aeolian dust samplers, Atmos.
800   Environ., 34, 1043-1057, 2000.

801   Goudie, A. and Middleton, N.: Saharan dust storms: nature and consequences, Earth Sci Rev., 56, 179-
802   204, 2001.

803   Holsen, T. M., Noll, K. E., Liu, S. P., and Lee, W. J.: Dry deposition of polychlorinated biphenyls in
804   urban areas, Environ. Sci. Technol. , 25, 1075-1081, 1991.

805   Huang, K., Zhuang, G., Li, J., Wang, Q., Sun, Y., Lin, Y., and Fu, J. S.: Mixing of Asian dust with
806   pollution aerosol and the transformation of aerosol components during the dust storm over China in
807   spring 2007, J Geophys Res Atmos, 115, 2010.

808   Jaenicke, R. and Junge, C.: Studien zur oberen Grenzgröße des natürlichen Aerosols, Contrib. Atmos.
809   Phys., 40, 129-143, 1967.

810   Jickells, T., An, Z., Andersen, K. K., Baker, A., Bergametti, G., Brooks, N., Cao, J., Boyd, P., Duce, R.,
811   and Hunter, K.: Global iron connections between desert dust, ocean biogeochemistry, and climate,
812   Science, 308, 67-71, 2005.

813   Junge, C.: Air Chemistry and Radioactivity. Academic Press, New York, 1963.

814   Kandler, K., Benker, N., Bundke, U., Cuevas, E., Ebert, M., Knippertz, P., Rodríguez, S., Schütz, L., and
815   Weinbruch, S.: Chemical composition and complex refractive index of Saharan Mineral Dust at Izana,
816   Tenerife (Spain) derived by electron microscopy, Atmos. Environ. , 41, 8058-8074, 2007.

817   Kandler, K., Schneiders, K., Ebert, M., Hartmann, M., Weinbruch, S., Prass, M., and Pöhlker, C.:
818   Composition and mixing state of atmospheric aerosols determined by electron microscopy: method
819   development and application to aged Saharan dust deposition in the Caribbean boundary layer, Atmos.
820   Chem. Phys., 18, 13429-13455, 2018.

821   Kandler, K., Schütz, L., Deutscher, C., Ebert, M., Hofmann, H., Jäckel, S., Jaenicke, R., Knippertz, P.,
822   Lieke, K., and Massling, A.: Size distribution, mass concentration, chemical and mineralogical
823   composition and derived optical parameters of the boundary layer aerosol at Tinfou, Morocco, during
824   SAMUM 2006, Tellus B, 61, 32-50, 2009.

825   Kandler, K., Schütz, L., Jäckel, S., Lieke, K., Emmel, C., Müller-Ebert, D., Ebert, M., Scheuvens, D.,
826   Schladitz, A., and Šegvić, B.: Ground-based off-line aerosol measurements at Praia, Cape Verde, during
827   the Saharan Mineral Dust Experiment: microphysical properties and mineralogy, Tellus B, 63, 459-474,
828   2011.

829   Lai, A. and Nazaroff, W.: Supermicron particle deposition from turbulent chamber flow onto smooth and
830   rough vertical surfaces, Atmos. Environ. , 39, 4893-4900, 2005.

831   López-García, P., Gelado-Caballero, M. D., Santana-Castellano, D., de Tangil, M. S., Collado-Sánchez,
832   C., and Hernández-Brito, J. J.: A three-year time-series of dust deposition flux measurements in Gran
833   Canaria, Spain: A comparison of wet and dry surface deposition samplers, Atmos. Environ., 79, 689-694,
834   2013.

835   Mendez, M. J., Funk, R., and Buschiazzo, D. E.: Efficiency of Big Spring Number Eight (BSNE) and
836   Modified Wilson and Cook (MWAC) samplers to collect PM10, PM2. 5 and PM1, Aeolian Res., 21, 37-
837   44, 2016.

838 Neto, E. C.: Speeding up non-parametric bootstrap computations for statistics based on sample moments
839 in small/moderate sample size applications, PLoS One, 10, e0131333, 2015.

840 Nicolas, M., Ndour, M., Ka, O., D'Anna, B., and George, C.: Photochemistry of atmospheric dust: ozone
841 decomposition on illuminated titanium dioxide, Environ. Sci. Technol., 43, 7437-7442, 2009.

842 Noll, K. E. and Fang, K. Y.: Development of a dry deposition model for atmospheric coarse particles,
843 Atmos. Environ., 23, 585-594, 1989.

844 Noll, K. E., Jackson, M. M., and Oskouie, A. K.: Development of an atmospheric particle dry deposition
845 model, Aerosol Sci. Technol. , 35, 627-636, 2001.

846 Ott, D. K., Cyrs, W., and Peters, T. M.: Passive measurement of coarse particulate matter, PM10–2.5, J.
847 Aerosol Sci 39, 156-167, 2008.

848 Ott, D. K. and Peters, T. M.: A shelter to protect a passive sampler for coarse particulate matter, PM10−
849 2.5, Aerosol Sci. Technol., 42, 299-309, 2008.

850 Penner, J. E., Andreae, M., Annegarn, H., Barrie, L., Feichter, J., Hegg, D., Jayaraman, A., Leaitch, R.,
851 Murphy, D., and Nganga, J.: Aerosols, their direct and indirect effects. In: Climate Change 2001: The
852 Scientific Basis. Contribution of Working Group I to the Third Assessment Report of the
853 Intergovernmental Panel on Climate Change, Cambridge University Press, 2001.

854 Piskunov, V.: Parameterization of aerosol dry deposition velocities onto smooth and rough surfaces, J.
855 Aerosol Sci, 40, 664-679, 2009.

856 Prospero, J. M., Schmitt, R., Cuevas, E., Savoie, D., Graustein, W., Turekian, K., Volz-Thomas, A., Diaz,
857 A., Oltmans, S., and Levy, H.: Temporal variability of summer-time ozone and aerosols in the free
858 troposphere over the eastern North Atlantic, Geophys. Res. Lett., 22, 2925-2928, 1995.

859 Rodríguez, S., Cuevas, E., Prospero, J., Alastuey, A., Querol, X., López-Solano, J., García, M., and
860 Alonso-Pérez, S.: Modulation of Saharan dust export by the North African dipole, Atmos. Chem. Phys.,
861 15, 7471-7486, 2015.

862 Sajjadi, H., Tavakoli, B., Ahmadi, G., Dhaniyala, S., Harner, T., and Holsen, T.: Computational fluid
863 dynamics (CFD) simulation of a newly designed passive particle sampler, Environ. Pollut. , 214, 410-
864 418, 2016.

865 Schlichting, H.: Boundary-layer theory, McGraw-Hill, 1968.

866 Schultz, E.: Größendifferenzierende Messung der Partikeldepositionsrate, Gefahrstoffe-Reinhalt. Luft. ,
867 49, 113-118, 1989.

868 Schulz, M., Prospero, J. M., Baker, A. R., Dentener, F., Ickes, L., Liss, P. S., Mahowald, N. M., Nickovic,
869 S., Garcia-Pando, C. P., and Rodríguez, S.: Atmospheric transport and deposition of mineral dust to the
870 ocean: implications for research needs, Environ. Sci. Technol. , 46, 10390-10404, 2012.

871 Shao, Y., Ishizuka, M., Mikami, M., and Leys, J.: Parameterization of size-resolved dust emission and
872 validation with measurements, J Geophys Res Atmos, 116, 2011.

873 Slinn, S. and Slinn, W.: Predictions for particle deposition on natural waters, Atmos. Environ., 14, 1013-
874 1016, 1980.

875 Tian, Z., Dietze, V., Sommer, F., Baum, A., Kaminski, U., Sauer, J., Maschowski, C., Stille, P., Cen, K.,
876 and Gieré, R.: Coarse-particle passive-sampler measurements and single-particle analysis by transmitted
877 light microscopy at highly frequented motorways, Aerosol Air Qual Res., 17, 1939, 2017.

878 VDI2119: Ambient air measurements sampling of atmospheric particles > 2.5μm on an acceptor surface
879 using the Sigma-2 passive sampler. Characterization by optical microscopy and calculation of number
880 settling rate and mass concentration. In: Verlag des Vereins Deutscher Ingenieure, Berlin, ICS:
881 13.040.01, Beuth Verlag, Berlin, 2013.

882 Wagner, J. and Leith, D.: Passive aerosol sampler. Part I: Principle of operation, Aerosol Sci. Technol. ,
883 34, 186-192, 2001a.

884 Wagner, J. and Leith, D.: Passive aerosol sampler. Part II: Wind tunnel experiments, Aerosol Sci.
885 Technol. , 34, 193-201, 2001b.

886 Wilson, S. J. and Cook, R. U.: Wind erosion. In: Soil Erosion M.J. Kirkby, a. R. P. C. M. (Ed.), 631.45
887 S6, John Wiley & Sons, Chichester, 1980.

888 WMO: GAW Report, 202. Workshop on Modelling and Observing the Impacts of Dust
889 Transport/Deposition on Marine Productivity (7-9 March 2011), Sliema, Malta, 2011.

890 Wood, N.: A simple method for the calculation of turbulent deposition to smooth and rough surfaces, J.
891 Aerosol Sci., 12, 275-290, 1981.

892 Xu, L., Mu, G., He, J., Yang, F., Ren, X., Wan, D., and Lin, Y.: Variability of dust mass concentrations
893 and deposition rates under different weather conditions in Cele Oasis, southern Tarim Basin, Environ.
894 Earth Sci., 75, 639, 2016.

895 Yamamoto, N., Hikono, M., Koyama, H., Kumagai, K., Fujii, M., and Yanagisawa, Y.: A passive sampler
896 for airborne coarse particles, J. Aerosol Sci, 37, 1442-1454, 2006.

897